

1 Evidence of Convective Redistribution of Carbon Monoxide in Aura Tropospheric  
2 Emission Sounder (TES) and Microwave Limb Sounder (MLS) Observations

3

4 M. Manyin, A. R. Douglass, M. R. Schoeberl

5

6 Michael Manyin

7 Science Systems and Applications, Inc., Lanham, Maryland, USA

8 Email: [Michael.Manyin@nasa.gov](mailto:Michael.Manyin@nasa.gov)

9 Address:

10 NASA/GSFC

11 Laboratory for Atmospheres

12 Code 613.3

13 Greenbelt, Maryland 20771

14

15 Anne Douglass

16 NASA Goddard Space Flight Center, Greenbelt, Maryland, USA

17 Email: [Anne.R.Douglass@nasa.gov](mailto:Anne.R.Douglass@nasa.gov)

18 Address:

19 NASA/GSFC

20 Laboratory for Atmospheres

21 Code 613.3

22 Greenbelt, Maryland 20771

23

24 Mark Schoeberl

25 Science and Technology Corporation, Hampton, Virginia, USA

26 Email: [Mark.Schoeberl@mac.com](mailto:Mark.Schoeberl@mac.com)

27 Address:

28 10005 Old Columbia Rd.

29 Suite M-150

30 Columbia, MD 21046

31

31 Abstract

32

33 Vertical convective transport is a key element of the tropospheric circulation.

34 Convection lofts air from the boundary layer into the free troposphere, allowing surface

35 emissions to travel much further, and altering the rate of chemical processes such as

36 ozone production. This study uses satellite observations to focus on the convective

37 transport of CO from the boundary layer to the mid and upper troposphere. Our

38 hypothesis is that strong convection associated with high rain rate regions leads to a

39 correlation between mid level and upper level CO amounts. We first test this hypothesis

40 using the Global Modeling Initiative (GMI) chemistry and transport model. We find the

41 correlation is robust and increases as the precipitation rate (the strength of convection)

42 increases. We next examine three years of CO profiles from the Tropospheric Emission

43 Sounder (TES) and Microwave Limb Sounder (MLS) instruments aboard EOS Aura.

44 Rain rates are taken from the Tropical Rainfall Measuring Mission (TRMM) 3B-42

45 multi-satellite product. Again we find a correlation between mid-level and upper

46 tropospheric CO, which increases with rain rate. Our result shows the critical importance

47 of tropical convection in coupling vertical levels of the troposphere in the transport of

48 trace gases. The effect is seen most clearly in strong convective regions such as the Inter-

49 tropical Convergence Zone.

50

51 1. Introduction/Background

52

53 Convection plays a vital role in tropospheric circulation as well as the distribution of  
54 trace gases. Surface level trace gas emissions are usually mixed within the atmospheric  
55 boundary layer (BL) via turbulent diffusion but are frequently blocked from entering the  
56 free troposphere (FT) by the inversion layer at the top of the BL. Convection, along with  
57 weather fronts and orographic processes, overcome the BL inversion trapping, moving air  
58 into the FT [*Liu et al.*, 2003]. Deep convection reaches the tropopause and sometimes  
59 even overshoots into the lower stratosphere. *Cotton et al.* [1995] estimated that  
60 convective (cloud related) processes vent the mass of the boundary layer tens of times  
61 over the course of a year.

62

63 Once convection lofts constituents into the FT, they can be transported intercontinental  
64 distances because of the consistent large scale flow in that region. Convection also  
65 contributes to inter-hemispheric transport: strong convergence from the Intertropical  
66 Convergence Zone (ITCZ) convective systems can draw air from both hemispheres and  
67 loft it high enough to be pulled into the Hadley circulation. In addition to these effects on  
68 transport, convection can also dramatically alter the rate of chemical processes because of  
69 its speed. Convective time scales are very short, on the order of hours for surface to UT,  
70 as opposed to days for synoptic scale processes. The rapid transport of chemical species  
71 means that short-lived species can still reach the upper troposphere. For example, when  
72 urban air with  $\text{NO}_x$  and other ozone precursors is quickly lofted to the FT, ozone  
73 production is greatly enhanced [*Pickering*, 1992] because the transport is fast compared  
74 to the  $\text{NO}_x$  lifetime. Convective transport also extends the lifetime of some species by

75 reducing their exposure to loss processes in the lower troposphere; this expands their  
76 range of chemical influence [*Dickerson et al.*, 1987].

77

78 Convective processes are complex, involving surface radiative heating, updrafts from  
79 lower tropospheric levels, detrainment at heights up to and above the tropopause,  
80 condensation, latent heat release, precipitation, downdrafts and evaporative cooling (e.g.  
81 *Gamache* [1982]). Other factors include melting ice particles, and turbulent mixing due to  
82 vertical shear and gravity wave instabilities. The scale of convective systems can range  
83 from isolated thunderstorms up to mesoscale complexes measuring 1000+ km. The  
84 wide-ranging impact of convection on chemical transport makes it crucial for us to  
85 quantify convective transport and evaluate its representation in models.

86

87 Previous studies of convection have focused on various features, including (i) showing  
88 evidence of convective transport from BL to upper troposphere/lower stratosphere region  
89 [*Poulida*, 1996; *Randel and Park*, 2006; *Li et al.*, 2005; *Park et al.*, 2007; *Ricaud et al.*,  
90 2007; *Ziemke et al.*, 2009] (ii) determining the height of convective outflow [*Gettelman*  
91 *and Forester*, 2002; *Froyd et al.*, 2009] (iii) identifying cases where outflow penetrates  
92 the tropopause, into the LS [*Hegglin*, 2004; *Ray et al.*, 2004; *Liu and Zipser*, 2005;  
93 *Chaboureau et al.*, 2007] (iv) comparing post-convective UT values measured by  
94 satellite to model predictions [*Liu et al.*, 2003; *Halland et al.*, 2009; *Mari et al.*, 2000]  
95 and (v) the diurnal cycle of convection [*Tian et al.*, 2004; *Liu and Zipser*, 2009].

96

97 One result which is especially pertinent to this study is the trimodal distribution of  
98 tropical clouds, which can be traced to levels of convective detrainment. *Johnson et al.*  
99 [1999] reported clouds forming at three main levels, as detected by shipborne radar  
100 during the TOGA COARE experiment: low cumulus near 2 km and cumulonimbus at 15  
101 to 16 km were most prominent, but cumulus congestus at approximately 5 km were  
102 frequent as well. These levels correspond well with stable layers associated with the trade  
103 wind inversion, the tropopause, and the 0°C melting level isotherm. Such stable levels are  
104 understood to be preferential regions of convective outflow (e.g. *Zuidema* [1998]). The  
105 mid-level cloud layer has also been documented by *Dessler et al.* [2006] using GLAS  
106 data, and by *Haynes and Stephens* [2007] and *Riley and Mapes* [2009] with CloudSat  
107 data. We will examine trace gas concentrations at the middle and upper levels of the  
108 trimodal distribution, to demonstrate the effects of convective transport.

109

110 The goal of this study is to use satellite measurements of CO combined with satellite-  
111 based locations of convective systems to quantify the impact of the convective systems  
112 on trace gas distributions. This study uses a 3 year archive of satellite data to search for  
113 evidence of convective transport of CO from the BL to mid and upper tropospheric  
114 levels. Observations are restricted to the tropics, where incoming solar radiation is  
115 strongest and convection is frequent. We use CO retrievals from the Tropospheric  
116 Emission Sounder (TES) on EOS Aura to detect mid-level concentrations, and CO  
117 retrievals from the Microwave Limb Sounder (MLS) aboard Aura for upper tropospheric  
118 values. To identify areas of convective transport we use estimates of rain rate derived

119 from microwave and IR satellite measurements, calibrated with Tropical Rainfall  
120 Measuring Mission (TRMM) observations, as a proxy for convective strength.  
121  
122 Carbon monoxide is a product of fossil fuel combustion and biomass burning, as well as  
123 the oxidation of hydrocarbons, particularly methane [Jacob, 1999]. As such, its highest  
124 concentrations are near the Earth's surface. CO is lost in the troposphere primarily by  
125 reaction with the hydroxyl radical OH. The lifetime of CO generally ranges between one  
126 and two months, depending on season and location within the atmosphere. Carbon  
127 monoxide is not soluble and therefore not subject to rainout. These qualities make it an  
128 excellent tracer. CO is monitored for many reasons, among which: it is a significant  
129 anthropogenic pollutant, it is a precursor to O<sub>3</sub> in the troposphere, and it is a sink for OH  
130 (thus modulating the oxidation of many greenhouse gases). Global CO measurements are  
131 currently provided by a number of space-borne instruments, including Measurements Of  
132 Pollution In The Troposphere (MOPITT) [Drummond, 1992] aboard the EOS Terra  
133 satellite, Atmospheric Infrared Sounder (AIRS) [McMillan *et al.*, 2005] aboard EOS  
134 Aqua, MLS [Waters *et al.*, 2006] and TES [Beer *et al.*, 2001], both on EOS Aura. We  
135 chose to use TES and MLS in this study: TES for its sensitivity in the mid-troposphere  
136 and its small footprint, allowing for unobscured profiles near or between clouds; MLS for  
137 its sensitivity near the tropopause, its capability to see through clouds, and its consistent  
138 proximity to TES profiles (as compared with MOPITT).  
139  
140 To locate convection, one must detect an accompanying phenomenon, such as clouds  
141 resulting from condensing of lofted water vapor, or rainfall from those clouds. Numerous

142 approaches to cloud characterization exist, including diagnosing outgoing longwave  
143 radiation (OLR) [*Liebmann and Smith, 1996; Lee et al., 2007*], GOES Precipitation Index  
144 (GPI) [*Arkin and Meisner, 1987*] based on microwave brightness temperatures, and  
145 International Satellite Cloud Climatology Project (ISCCP) cloud classification [*Rossow  
146 and Schiffer, 1991*] based on cloud top pressure and optical depth. Techniques such as  
147 OLR and ISCCP yield high resolution products, but global coverage is only once or twice  
148 a day. GPI and its derivatives use data from geosynchronous satellites for good spatial  
149 and temporal resolution, but features such as high cirrus and non-raining portions of  
150 cloud anvils pose difficulties.

151

152 Microwave instruments that can detect precipitation beneath clouds are quite effective at  
153 locating convective rainfall. Successful estimation of rain rate from passive microwave  
154 satellite data was first demonstrated with ESMR on Nimbus satellites [*Wilheit et al.,  
155 1973*]. Current sensors include SSM/I on DMSP spacecraft, and TMI and PR aboard  
156 TRMM. Product resolution is quite good, but coverage is incomplete.

157 Algorithms such as the TRMM 3B-42 (see section 2.2) estimate rain rates with  
158 microwave data where available and calibrated IR data elsewhere, in addition to rain  
159 gauge values. This provides full coverage in the low and mid latitudes, every 3 hours, at  
160 quarter degree resolution. We presume that higher rain rates from the TRMM 3B-42  
161 product imply greater likelihood of convection.

162

163 2. Approach

164

165 The coupling of the BL and FT by convection should have a definite signature in the  
166 trace gases. CO should appear aloft following a convective event that ventilates the BL,  
167 and outflow levels in the mid and upper troposphere should both show evidence of this  
168 lofting transport, since detrainment preferentially occurs near the stable layers of 0°C  
169 (occurring between 500 and 600 hPa) and the tropopause (~200 hPa). Thus there should  
170 be higher correlation between trace gas concentrations at mid and upper tropospheric  
171 levels following periods of local convective activity.

172

173 Our approach is to examine correlations between concentrations of CO in the middle and  
174 upper troposphere, and relate them to proximity to significant rainfall. First we examine  
175 this relationship within the context of a numerical model, the Global Modeling Initiative  
176 (GMI) chemistry and transport model (CTM). Using this model will allow us to examine  
177 what might be observed at the model scale of 2.5° longitude x 2° latitude. Then we  
178 search for a similar relationship using data from TES and MLS on Aura. We use TES  
179 pressure level 562 hPa and MLS level 215 hPa, because these correspond well with  
180 convective detrainment levels put forth in the trimodal cloud characterization [*Johnson et*  
181 *al.*, 1999]. We use the TRMM-calibrated 3B-42 rain rate product to identify likely  
182 instances of convection.

183

184 One challenge of using TES observations is that moist convection is accompanied by  
185 clouds, which prevent infrared-based remote sensing of the lower atmosphere. We  
186 anticipated however that cloud-free observations of the middle troposphere would be  
187 available immediately adjacent to convective areas, e.g. between clouds or along the



188 edges of convective storms. The small TES footprint makes this approach reasonable.  
189 We anticipate only a small fraction of the ~650 measurements made in the tropics (18°N-  
190 S) during each global survey will meet our criteria for cloud amount and proximity to  
191 convection. We compensate for infrequency by drawing upon a multi-year archive.

192

193 The remainder of the paper is structured as follows: The models (CTM and AGCM) are  
194 discussed in section 2.1; the data sources for CO and rain rate are presented in 2.2.

195 Results are given in section 3, and conclusions follow in section 4.

196

197 2.1 GMI and GEOS-4

198

199 NASA's Global Modeling Initiative has developed a 'Combo' CTM that combines  
200 photochemical schemes that are appropriate for the stratosphere and troposphere. The  
201 Combo CTM may be driven by meteorological fields from a general circulation model  
202 (GCM) or from a data assimilation system (DAS). GMI Combo includes gas phase  
203 reactions, photolysis, wet scavenging, dry deposition, heterogeneous chemistry (PSCs)  
204 and emissions [*Strahan et al.*, 2007; *Duncan et al.*, 2007]. For this study we have used  
205 the "Aura4" GMI experiment, run at 2° latitude by 2.5° longitude, with 55 vertical levels  
206 (hybrid sigma-pressure) up to 0.015 hPa. We use simulated CO that is recorded at times  
207 corresponding to the Aura afternoon overpass times, between 1 and 2 p.m. local time to  
208 best match the observation times of TES on Aura.

209

210 For the Aura4 experiment, GMI ‘Combo’ used meteorological fields taken from the  
211 Goddard Earth Observing System Data Assimilation System (GEOS DAS) version 4  
212 [*Bloom et al.*, 2005]. The GEOS DAS fields are produced at 1° latitude by 1.25°  
213 longitude on 55 levels; the fields are adapted for use at 2° by 2.5° in the CTM. The  
214 physics parameterization scheme consists of parameterizations for precipitation,  
215 clouds/radiation, turbulent mixing, and surface processes. The deep moist convection  
216 scheme is that of *Zhang and McFarlane* [1995], which uses a plume ensemble approach  
217 with convective updrafts and related downdrafts. Shallow convection is covered by the  
218 *Hack* [1994] scheme.

219

220 GEOS-4 DAS assimilates observations from many sources, including SSM/I (total  
221 precipitable water), MODIS (winds), geosynchronous satellites (winds), TOVS sounders  
222 (temperature and moisture), ERS-2 and QuikScat (sea-level winds), along with  
223 rawinsondes (temperature, winds, moisture), and surface stations (temperature, pressure,  
224 winds). The DAS outputs dozens of fields, including those that GMI requires, such as  
225 winds, temperature, precipitation and convective mass flux. Fields are saved at three  
226 hour intervals, in instantaneous and time-averaged forms; GMI ‘Combo’ uses the latter,  
227 horizontally averaged to 2° x 2.5°. In order to identify grid boxes with convective  
228 activity, we used the GEOS-4 DAS output field “PRECON”, which stores the convective  
229 precipitation rate. Each GEOS-4 output file covers a single synoptic time period. In  
230 order to match the local ascending Aura overpass times implicit in each GMI output file,  
231 the convective precipitation field had to be extracted from multiple GEOS-4 files  
232 covering 24 hours of simulation.

233

234 2.2 TES, MLS and TRMM (3B-42)

235

236 The Tropospheric Emission Spectrometer (TES) is a Fourier transform spectrometer  
237 [*Beer et al.*, 2001; *Beer*, 2006]. It is one of several instruments aboard NASA's Aura  
238 satellite, positioned in an ascending sun synchronous orbit with equator crossing at about  
239 13:45 local solar time. TES measures in the infrared to detect trace gases including CO,  
240 water vapor, O<sub>3</sub> and methane. This study uses nadir profiles acquired during TES Global  
241 Surveys. Nadir view operates with a 5.3 x 8.3 km footprint, and each profile in a Level 2  
242 file consists of data on 65 pressure levels ranging from nominal surface pressure to 0.1  
243 hPa. Compared to the GMI model, TES has a much higher horizontal resolution, but of  
244 course the TES observations are much sparser than the GMI output (e.g. 9800 tropical  
245 profiles in July 2007, compared with 84,816 GMI gridbox values). And in terms of  
246 vertical resolution, the model levels within a grid column are independent compared to  
247 low vertical resolution retrieved TES profiles.

248

249 In the tropics, a TES tropospheric CO profile typically has between 1 and 2 degrees of  
250 freedom (DOF), a measure of the number of "independent" pieces of information that  
251 contributed to that profile. These pieces of information are used to modify the a priori  
252 (first guess) trace gas profile. (See *Beer* [2006] for an overview.) With a greater number  
253 of DOFs it is possible to achieve more variation from the a priori. In December 2005,  
254 TES implemented an Optical Bench warmup which resulted in better instrument

255 alignment, and average DOF values for TES CO measurements were significantly  
256 improved. For this reason, we have only used data from January 2006 forward.

257

258 As a consequence of variations in TES DOF, some measurements reflect the actual state  
259 of the atmosphere, while others rely heavily on the a priori. To distinguish between such  
260 cases we consult the averaging kernel diagonal (AKD) values; where these are high  
261 (close to 0.1), there is greater confidence that the true atmospheric values are retrieved  
262 [Halland *et al.*, 2009]. We tested several AKD thresholds and use an AKD threshold of  
263 0.085 for most of this paper. In the final figure we show results using two other  
264 thresholds for the AKD.

265

266 TES profiles used in this study were Level 2, Version 4. They were filtered using the  
267 quality control fields, as in Table 5-3 of the *EOS TES L2 Data User's Guide* [Osterman  
268 *et al.*, 2008]. In addition, since the TES IR-based retrievals are subject to interference by  
269 clouds, profiles with nominal cloud top pressures less than 572 hPa were discarded. We  
270 used profiles between 18°N and 18°S because DOFs changed abruptly beyond those  
271 boundaries due to changes in the a priori.

272

273 The MLS instrument aboard Aura measures profiles of radiance from the Earth's limb  
274 from upper troposphere to the mesosphere [Waters, 2006]. MLS scans columns ahead of  
275 the satellite, every 165km along its orbit. MLS measures CO [Livesey *et al.*, 2006;  
276 Pumphrey *et al.*, 2007], along with a dozen other atmospheric trace gases. As a

277 microwave instrument, it can detect constituents despite the presence of aerosols, cirrus  
278 or polar stratospheric clouds.

279

280 In this study we use CO as reported by MLS (version 2.2) at 215 hPa. At this level, the  
281 CO morphology and variability are adequately measured, but the values are biased by  
282 approximately a factor of 2 [*Livesey et al.*, 2008]. We compensate by dividing all values  
283 in half; we also processed the data according to guidelines in the MLS data quality  
284 document [*Livesey et al.*, 2007]. Each MLS CO profile was paired with the closest TES  
285 profile; the average separation was 195 km, and the average time difference was  
286 approximately 7 minutes.

287

288 For rain rate data, we turned to the 3B-42 product from the Tropical Rainfall Measuring  
289 Mission (TRMM) [*Simpson et al.*, 1996]. This mission, a joint effort of the United States  
290 and Japan, was launched in 1997. It supports several instruments including the TRMM  
291 Microwave Imager (TMI), the Precipitation Radar (PR), and the Visible and Infrared  
292 Scanner (VIRS) [*Kummerow et al.*, 1998]. The 3B-42 algorithm [*Huffman et al.*, 2007]  
293 combines observations from several satellites, including TRMM, with rain gauge  
294 analyses. Computation of the multi-satellite portion begins with a merged microwave  
295 product including TMI and SSM/I rain rate estimates. Then VIRS data is used to produce  
296 an infrared/rain rate relationship, which is applied to geosynchronous IR data, such as  
297 that from the Geostationary Operational Environmental Satellite (GOES) series. The  
298 microwave products are high resolution (e.g. TMI is 5.1 km), but measurements  
299 accumulated over timescales of up to three hours do not completely cover the tropics.

300 The IR measurements are similar resolution (e.g. GOES is 4 km), and a merged product  
301 from several geo-IR satellites provides excellent coverage (60° N-S) at half hour intervals  
302 [*Janowiak et al.*, 2001]. Incorporating both microwave and IR data, the 3B-42 rain rate  
303 product is generated for latitudes covered by TRMM (50° N-S) at quarter degree  
304 resolution and 3 hour intervals.

305

306 3B-42 does not distinguish between convective rain, which is linked to strong vertical  
307 transport, and stratiform rain, which is not. However, it is generally true that greater rain  
308 rates are more likely associated with convective systems. Indeed, the ratio of convective  
309 to stratiform rain rates in the tropics is 4.1, when measured at PR resolution [*Schumacher*  
310 *and Houze*, 2003]. So the error introduced by the inclusion of stratiform rain rates in this  
311 study should be relatively small.

312

313 Rain rates were used as follows: For a given pair of TES and MLS CO profiles we  
314 searched a neighborhood of 3B-42 grid boxes centered on the spot midway between the  
315 profiles. Since 3B-42 rain rates are available every three hours, we used the values from  
316 the 3-hour window prior to the TES observation, to ensure that we would see the effects  
317 of vertical mixing.

318

319 3. Results

320

321 3.1 GMI and GEOS-4

322

323 We first analyze simulated upper and mid-tropospheric CO to demonstrate the expected  
324 relationship between composition and convective transport as implemented in the GMI  
325 CTM.

326

### 327 3.1.1 Scatter plots varying rain rate threshold

328

329 Daily GMI CO concentrations from July 2007 were compared at two different pressure  
330 levels, 562 hPa and 215 hPa, selected to match the TES and MLS pressure levels used in  
331 the next section. The 562 hPa level represents the level of expected convective  
332 detrainment around the 0°C isotherm, while 215 hPa corresponds with outflow near the  
333 tropopause. As shown in the first scatter plot of Figure 1, the majority of CO values on  
334 both pressure levels range between 50 and 150 ppbv. Panel (a) includes values from all  
335 GMI grid boxes in the tropics, 19°S - 19°N, regardless of rain rate. The broad pattern  
336 matches our expectations: Points along the diagonal are consistent with vertical  
337 convective transport to both levels of the troposphere; areas with substantial CO at lower  
338 altitudes but minimal amounts above may represent cases where shallow convection has  
339 deposited CO emissions from the boundary layer up into the mid-troposphere. Areas  
340 with greater CO concentrations at 215 hPa may represent cases where deep convection  
341 has been dominant. The off-diagonal cases could also be due to the effects of horizontal  
342 advection transporting CO from other convective areas.

343

344 Figure 1, panels (b)-(d) show subsets of the original data, where profiles were discarded  
345 if the convective rain rate was less than 0.5, 1.0 and 2.0 mm/hr respectively. As

346 convective activity increases from one panel to the next, profiles with markedly different  
347 CO concentrations at the two levels are eliminated. This fits with our hypothesis, in that  
348 convective transport is coupling the middle and upper levels of the troposphere. In the  
349 last panel, where convective rain rates are highest, the remaining points are clustered  
350 along the diagonal, and the correlation coefficient is quite high, at 0.967. This simple test  
351 demonstrates that the GMI implementation of trace gas transport, as driven by GEOS-4  
352 winds and convective mass flux, is consistent with our conceptual model of the effect  
353 vertical convective mixing will have on the trace gas distributions. This is an idealized  
354 case with which to compare the TES/MLS observations.

355

### 356 3.1.2 Geographic Location of GEOS-4 Rain

357

358 Another useful plot for comparing the model and satellite results is the geographic  
359 location of dominant rainfall. The areas of convective rain in the GEOS-4 DAS are  
360 shown in Figure 2. The grid boxes are shaded based on the number of days that met or  
361 exceeded the rain rate threshold. Note the prominence of the ITCZ in panels (a) and (b),  
362 and the areas of most frequent convective rain such as Costa Rica and north of Papua  
363 New Guinea, in panel (c). These plots confirm the success of GEOS-4 DAS in  
364 reproducing realistic rain distribution patterns.

365

### 366 3.2 TES, MLS and TRMM (3B-42)

367



368 The TES and MLS observations are quite sparse in comparison to model output. Within  
369 our constraints of tropical latitudes and sufficiently cloud-free observations, a month of  
370 TES Global Survey data yields roughly 30 to 60 profiles. Filtering these using rain rate  
371 thresholds quickly reduces the sample size to numbers too small for a meaningful  
372 analysis. So we chose to include three full years of TES and MLS data in this study,  
373 from 2006 through 2008.

374

375 In order to estimate the strength of convection in the neighborhood of TES and MLS  
376 measurements, we consulted the TRMM-calibrated rain rate data for the 3-hour interval  
377 prior to the TES overpass time. Our initial tests included an area similar in size to a GMI  
378 gridbox: we searched an 11x7 patch of TRMM values centered between the TES and  
379 MLS profiles, and took the maximum rain rate. (Since TRMM 3B-42 is 0.25° resolution,  
380 the area was 2.75° in longitude by 1.75° in latitude.) In addition we tested our approach  
381 with smaller patches of TRMM grid boxes, including 7x5, 5x3 and 3x3. As the area in  
382 which we searched for rain grew smaller, the effects of the vertical mixing became more  
383 apparent. So we begin by examining the 3x3 case, wherein each patch is a square of 9  
384 grid boxes; the maximum rain rate is sought within a 0.75° x 0.75° region.

385

386 3.2.1 Scatter plots varying rain rate thresholds

387

388 Plots of CO correlation between pressure levels 562 and 215 hPa are shown in Figure 3.  
389 Panel (a) includes all qualifying profiles, regardless of local rain rate. It shows that the  
390 majority of values at midlevel are between 50 and 150 ppbv, while the range on the upper

391 level is between 50 and 125 ppbv. The (solid) line of linear fit shows that greater CO  
392 concentrations exist at lower altitudes. This can be attributed to diffusive transport from  
393 the boundary layer, particularly during times of weak trade inversion. It may also be due  
394 in part to the approximate correction we have applied to compensate for the MLS high  
395 bias. Greater CO concentrations at mid-level were also present in GMI (see the line of  
396 linear fit in Figure 1), but in the TES/MLS case this is much more pronounced.

397

398 Panels (b)-(d) in Figure 3 show the relationship between middle and upper tropospheric  
399 CO as the rain rate requirement for the TES/MLS observation neighborhood is increased.  
400 As the threshold is increased from 1 up to 3 mm/hr, the correlation steadily increases as  
401 well. TES/MLS values associated with higher rain rates are clustered around the  
402 diagonal, as was the case in the GMI plots (Figure 1). Clustering is tighter for GMI,  
403 because values are reported immediately after the convective mass flux is applied to the  
404 trace gas field, as opposed to the TES/MLS measurements which were taken up to 6  
405 hours after rainfall. The interval between convective rain and CO observations gives  
406 advection time to alter distributions.

407

408 Part of the difficulty in characterizing patterns in this data is the remarkably low number  
409 of profiles satisfying our criteria, as shown in Table 1. This is due in part to the rejection  
410 of cloudy TES profiles. For the 0 mm/hr case, 84% of the profiles were filtered out based  
411 on their cloud top pressure. In the case of 3 mm/hr, 90% were removed. The linkage of  
412 additional clouds with higher rain rate was expected, since convective rain is  
413 accompanied by updrafts, leading to detrainment, condensation, and therefore clouds.

414

415 To establish a level of confidence in the correlation values computed for small sample  
416 sizes, we employed a bootstrap approach: we computed the correlation for a randomly  
417 chosen subset of half the points, repeated this process 1000 times, and made histograms  
418 of the results. We accepted the correlation over the full sample only when it matched the  
419 average of the bootstrap correlations to within 0.05, and when the central 90% of the  
420 bootstrap values did not exceed a range of 0.5. Each of the correlations listed in Table 1  
421 satisfied these criteria. The bootstrap histograms are shown as insets in Figure 3, with  
422 markers denoting the 5%, 95% and average values.

423

### 424 3.2.2 Geographic Location of TES/MLS Observations

425

426 Because strong convection is usually accompanied by substantial clouds, we anticipated  
427 that non-cloudy TES profiles linked with higher rain rates would be adjacent to regions of  
428 heavy rain, rather than within such regions. The locations of accepted TES/MLS profile  
429 pairs are shown in Figure 4. In panel (a), rain rates are not considered, and the pattern  
430 arises solely from the elimination of cloudy profiles. The areas of highest number of  
431 observations are those that tend to have low levels of rain, such as Saudi Arabia and the  
432 horn of Africa. The fewest profiles are found in areas of high rainfall, such as the ITCZ,  
433 Maritime Continent, Indian Ocean and Brazil. So, as expected, most non-cloudy TES  
434 observations are in the areas of least convective rain. Once a rain rate threshold is  
435 applied a different pattern emerges. (Note that the color scale for panels (b) and (c) is  
436 different from that in the first panel.) As anticipated, the profiles in rainy neighborhoods

437 tend to be located adjacent to areas of frequent rain, such as the ITCZ, Brazil, and the  
438 Indian Ocean. We interpret these to be instances where TES measures CO in sufficiently  
439 cloud-free columns along the edges of convective storm systems. The convective lofting  
440 of CO by such systems is evident in the TES and MLS data. With higher rain rates there  
441 is greater likelihood of convective activity in the area, and therefore greater vertical  
442 mixing of CO and higher correlation between levels.

443

### 444 3.2.3 Correlation affected by size of TRMM neighborhood, and AK Diagonal

445

446 How does the correlation between mid and upper levels of CO change as the distance  
447 from convection increases? And how is the correlation affected by our choice of AKD  
448 threshold? To answer these questions, we performed two sensitivity experiments. First  
449 we varied the size of the search neighborhood in the TRMM-based rain rate data, testing  
450 four different patch sizes: 11x7, 7x5, 5x3 and 3x3 grid boxes, in the 0.25° x 0.25° grid.  
451 Larger search areas allow for rain rate maxima to be identified at greater distances from  
452 the CO profiles. In the second sensitivity test we varied the minimum TES AKD  
453 accepted: 0.08, 0.085 and 0.09. This was done to determine the trend in correlations as  
454 TES values gained greater independence from the a priori and more accurately reflected  
455 the state of the atmosphere. The results from both of these experiments are shown in  
456 Figure 5. Multiple patch sizes are plotted in each panel, and a different minimum AKD  
457 applies to each panel. (Note that the original series of correlations, recorded in Table 1,  
458 appears as the sequence of red asterisks in the middle panel.)

459

460 The influence of TRMM search area size is evident in panel (a). Each gray square  
461 designates the CO correlation derived from TES/MLS profile pairs close to a sufficiently  
462 high TRMM rain rate, determined by searching an 11x7 neighborhood of TRMM values  
463 ( $2.75^\circ \times 1.25^\circ$ ). The blue triangles show the results from searching smaller  
464 neighborhoods of 7x5 grid boxes ( $1.75^\circ \times 1.25^\circ$ ). The green diamonds reflect 5x3 patches  
465 ( $1.25^\circ \times 0.75^\circ$ ), and the red asterisks use 3x3 patches ( $0.75^\circ \times 0.75^\circ$ ).

466 As the search area is constricted, the average distance between the TES/MLS profiles and  
467 maximum rain rate is reduced, so the lofting effects of convection should be more evident  
468 in the CO measurements, and we anticipated higher correlation as a result. This is clearly  
469 exhibited in the plots; while the 11x7 sequence does not show an increase in correlation  
470 as local maximum rain rate increases, the 7x5 sequence does show this relationship, and  
471 the 5x3 and 3x3 cases even more so. This demonstrates that trace gas correlation between  
472 the middle and upper troposphere depends on proximity to convection as well as  
473 convective intensity.

474

475 The series of three panels shows the impact of more stringent TES AKD requirements.  
476 Two effects are apparent. First, as average AKD increases, the CO correlation for a given  
477 rain rate tends to increase as well. This means that the trends we are seeing derive  
478 primarily from the atmospheric state, and should not be attributed to the TES a priori.  
479 The second effect is the reduction in qualified TES profiles, resulting in smaller sample  
480 sizes over which to evaluate correlations. This paucity of data is further exacerbated  
481 when profiles are filtered based on rain rate. With  $\text{TES AKD} \geq 0.08$ , before rain rate is  
482 considered, there are 17,358 profile pairs from the 2006-2008 period; with  $\text{AKD} \geq 0.085$

483 there are 9,945 pairs, and with  $AKD \geq 0.09$  only 5,091 pairs qualify. Filtering these sets  
484 with increasing rain rate thresholds quickly reduces the sample sizes to fewer than 50,  
485 and soon thereafter the bootstrap confidence test (see section 3.2.1) begins to fail,  
486 discontinuing each sequence. For example, the 3x3 sequence in panel (c) is computed for  
487 rain rates at or above 0, 0.5 and 1.0 mm/hr, using 5,091, 83 and 41 profile pairs  
488 respectively. At 1.5 mm/hr, too few profiles remain to calculate a statistically meaningful  
489 correlation. We assert that, despite the short series of correlations plotted in the last panel,  
490 they confirm the trends seen in the prior two panels, namely that the proximity and  
491 intensity of convection influences the degree of correlation in middle and upper  
492 tropospheric concentrations of CO.

493

#### 494 4. Conclusion

495

496 Using rain activity as a proxy for convection we have demonstrated a link between  
497 tropical convection and CO concentrations in the middle and upper troposphere, at levels  
498 corresponding to the stable layers at 0°C and the tropopause. In other words, convective  
499 activity is pumping CO from the surface into the mid and upper troposphere – chemically  
500 coupling the tropospheric layers. This association was first demonstrated in the GMI  
501 CTM. Correlations between CO concentrations at 562 and 215 hPa increased as the  
502 convective precipitation rate increased. This conformed to our expectations. In addition,  
503 the locations of high convective rain rates for the month we studied aligned well with  
504 standard patterns of tropical rain, e.g. the ITCZ.

505

506 For the observational study, CO measurements from TES at 562 hPa (unobscured by  
507 clouds) and from MLS at 215 hPa were examined, together with rain rates from the  
508 TRMM 3B-42 product. First we examined the influence of rain rate on the correlation,  
509 using a 0.75 x 0.75 search area within TRMM data for each pair of TES/MLS profiles,  
510 and using TES profiles with at least an AKD value of 0.085. As the rain rate threshold  
511 was increased, the correlation between CO burdens at the two levels grew stronger, as we  
512 anticipated; greater convective vertical mixing is concomitant with heavier rain.  
513 However, the sample size (profile count) fell dramatically as we restricted ourselves to  
514 higher local rain rates. This was because rain is accompanied by clouds (convective rain  
515 leads to additional cloud formation), and we discarded TES profiles that were not  
516 sufficiently cloud-free.

517

518 The influence of clouds was also evident in the location of qualifying profiles. Most  
519 profiles clustered in areas of minimal rain, such as the horn of Africa. When rain rate  
520 thresholds were enforced, the remaining profiles appeared at the periphery of major  
521 cloudy areas such as the ITCZ and Brazil. These plots differed greatly from the GMI  
522 location plots, principally due to the cloud-free condition we imposed on TES profiles.  
523 Fortunately, the small footprint of TES permitted some measurements not obscured by  
524 clouds immediately adjacent to regions with rain. We extended the study to include 36  
525 months of data to provide a sufficient number of non-cloudy profiles. Also we used a  
526 bootstrap statistical method to gauge confidence in cases with only a small number of CO  
527 measurements. By these means we were able to show linkage between rain rate and CO  
528 burden correlation similar to that shown with the model.

529

530 We explored the sensitivity of this result to two parameters: the rain search area, and the  
531 TES averaging kernel diagonal values. For the former, we varied the extent of search  
532 within TRMM 3B-42 for a maximum rain rate to associate with each TES/MLS profile  
533 pair. TRMM data neighborhoods of four sizes, ranging from  $2.75^{\circ} \times 1.75^{\circ}$  (approximately  
534 the size of one GMI gridbox), to  $0.75^{\circ} \times 0.75^{\circ}$  were tested. For each areal size, our first  
535 result was reproduced: increased rain rates led to higher correlations. Smaller search  
536 domains also tended to yield better correlations, particularly for greater rain rates. This  
537 result is consistent with the idea that closer proximity to convective mixing translates into  
538 a stronger observable signal. When we required higher AKD values for TES, the  
539 correlations again tended to rise, giving us confidence that the signal in CO reflected  
540 actual atmospheric concentrations, rather than strong influence from the a priori. We  
541 showed significant correlations up to AKD threshold 0.09, beyond which the profile  
542 count was too small for meaningful results.

543

544 We have demonstrated that tropical convection plays an important role in transporting  
545 trace gases vertically within the troposphere, with effects in keeping with the trimodal  
546 characterization of tropical clouds, in which boundary layer parcels are convectively  
547 lofted to stable levels in the troposphere. Satellite observations show that this process  
548 operates on a wide scale throughout the tropical regions where strong convection is  
549 prevalent.

550



551 In this paper we examined how correlation was affected by proximity to rainfall but  
552 subsequent advection of the CO plume was not considered. A follow-up study could  
553 focus on cases where convection was located upwind of the CO measurement.

554

555

556 Acknowledgements

557

558 We would like to thank Susan Strahan for her assistance with GMI, and George Huffman  
559 who provided guidance on using the TRMM 3B-42 product.

560

561 The TES data were obtained from the NASA Langley Research Center Atmospheric  
562 Sciences Data Center.

563

564

565 References

566

567 Arkin, P. A., and B. N. Meisner (1987), THE RELATIONSHIP BETWEEN LARGE-  
568 SCALE CONVECTIVE RAINFALL AND COLD CLOUD OVER THE WESTERN-  
569 HEMISPHERE DURING 1982-84, *Monthly Weather Review*, 115(1), 51-74.

570

571 Beer, R. (2006), TES on the Aura mission: Scientific objectives, measurements, and  
572 analysis overview, *Ieee Transactions on Geoscience and Remote Sensing*, 44(5), 1102-  
573 1105, DOI:10.1109/tgrs.2005.863716.

574

575 Beer, R., T. A. Glavich, and D. M. Rider (2001), Tropospheric emission spectrometer for  
576 the Earth Observing System's Aura Satellite, *Applied Optics*, 40(15), 2356-2367.

577

578 Bloom, S., et al. (2005), Documentation and Validation of the Goddard Earth Observing  
579 System (GEOS) Data Assimilation System-Version 4 *Rep.*

580

581 Chaboureau, J. P., J. P. Cammas, J. Duron, P. J. Mascart, N. M. Sitnikov, and H. J.

582 Voessing (2007), A numerical study of tropical cross-tropopause transport by convective  
583 overshoots, *Atmospheric Chemistry and Physics*, 7(7), 1731-1740.

584

585 Cotton, W. R., G. D. Alexander, R. Hertenstein, R. L. Walko, R. L. McAnelly, and M.

586 Nicholls (1995), Cloud venting - A review and some new global annual estimates, *Earth-*  
587 *Science Reviews*, 39(3-4), 169-206.

588

589 Dessler, A. E., S. P. Palm, and J. D. Spinhirne (2006), Tropical cloud-top height

590 distributions revealed by the Ice, Cloud, and Land Elevation Satellite

591 (ICESat)/Geoscience Laser Altimeter System (GLAS), *Journal of Geophysical Research-*  
592 *Atmospheres*, 111(D12), 11, DOI: D12215 10.1029/2005jd006705.

593

594 Dickerson, R. R., et al. (1987), THUNDERSTORMS - AN IMPORTANT

595 MECHANISM IN THE TRANSPORT OF AIR-POLLUTANTS, *Science*, 235(4787),

596 460-464.

597

598 Drummond, J. R. (1992), Measurements of Pollution in the Troposphere (MOPITT)*Rep.*,  
599 77-101 pp, North-Holland, Amsterdam.

600

601 Duncan, B. N., S. E. Strahan, Y. Yoshida, S. D. Steenrod, and N. Livesey (2007), Model  
602 study of the cross-tropopause transport of biomass burning pollution, *Atmospheric*  
603 *Chemistry and Physics*, 7(14), 3713-3736.

604

605 Froyd, K. D., D. M. Murphy, T. J. Sanford, D. S. Thomson, J. C. Wilson, L. Pfister, and  
606 L. Lait (2009), Aerosol composition of the tropical upper troposphere, *Atmospheric*  
607 *Chemistry and Physics*, 9(13), 4363-4385.

608

609 Gamache, J. F., and R. A. Houze (1982), MESOSCALE AIR MOTIONS ASSOCIATED  
610 WITH A TROPICAL SQUALL LINE, *Monthly Weather Review*, 110(2), 118-135.

611

612 Gettelman, A., and P. M. D. Forster (2002), A climatology of the tropical tropopause  
613 layer, paper presented at International Symposium on Stratospheric Variations and  
614 Climate, Fukuoka, Japan, Nov 12-15.

615

616 Hack, J. J. (1994), Parameterization of moist convection in the National Center for  
617 Atmospheric Research community climate model (CCM2), *Journal of Geophysical*  
618 *Research-Atmospheres*, 99(D3), 5551-5568.

619

620 Halland, J. J., H. E. Fuelberg, K. E. Pickering, and M. Luo (2009), Identifying convective  
621 transport of carbon monoxide by comparing remotely sensed observations from TES with  
622 cloud modeling simulations, *Atmospheric Chemistry and Physics*, 9(13), 4279-4294.

623

624 Haynes, J. M., and G. L. Stephens (2007), Tropical oceanic cloudiness and the incidence  
625 of precipitation: Early results from CloudSat, *Geophysical Research Letters*, 34(9), 5,  
626 DOI: L09811 10.1029/2007gl029335.

627

628 Hegglin, M. I., et al. (2004), Tracing troposphere-to-stratosphere transport above a mid-  
629 latitude deep convective system, *Atmospheric Chemistry and Physics*, 4, 741-756.

630

631 Huffman, G. J., R. F. Adler, D. T. Bolvin, G. J. Gu, E. J. Nelkin, K. P. Bowman, Y.

632 Hong, E. F. Stocker, and D. B. Wolff (2007), The TRMM multisatellite precipitation  
633 analysis (TMPA): Quasi-global, multiyear, combined-sensor precipitation estimates at  
634 fine scales, *Journal of Hydrometeorology*, 8(1), 38-55, DOI: 10.1175/jhm560.1.

635

636 Jacob, D. J. (1999), *Introduction to Atmospheric Chemistry*, Princeton University Press,  
637 Princeton, New Jersey.

638

639 Janowiak, J. E., R. J. Joyce, and Y. Yarosh (2001), A real-time global half-hourly pixel-  
640 resolution infrared dataset and its applications, *Bulletin of the American Meteorological*  
641 *Society*, 82(2), 205-217.

642

- 643 Johnson, R. H., T. M. Rickenbach, S. A. Rutledge, P. E. Ciesielski, and W. H. Schubert  
644 (1999), Trimodal characteristics of tropical convection, *Journal of Climate*, 12(8), 2397-  
645 2418.
- 646
- 647 Kummerow, C., W. Barnes, T. Kozu, J. Shiue, and J. Simpson (1998), The Tropical  
648 Rainfall Measuring Mission (TRMM) sensor package, *Journal of Atmospheric and*  
649 *Oceanic Technology*, 15(3), 809-817.
- 650
- 651 Lee, H. T., A. Gruber, R. G. Ellingson, and I. Laszlo (2007), Development of the HIRS  
652 outgoing longwave radiation climate dataset, *Journal of Atmospheric and Oceanic*  
653 *Technology*, 24(12), 2029-2047, DOI: 10.1175/2007jtecha989.1.
- 654
- 655 Li, Q. B., et al. (2005), Convective outflow of South Asian pollution: A global CTM  
656 simulation compared with EOS MLS observations, *Geophysical Research Letters*,  
657 32(14), DOI: L14826 10.1029/2005gl022762.
- 658
- 659 Liebmann, B., and C. A. Smith (1996), Description of a complete (interpolated) outgoing  
660 longwave radiation dataset, *Bulletin of the American Meteorological Society*, 77(6),  
661 1275-1277.
- 662
- 663 Liu, C. T., and E. J. Zipser (2005), Global distribution of convection penetrating the  
664 tropical tropopause, *Journal of Geophysical Research-Atmospheres*, 110(D23), DOI:  
665 D23104 10.1029/2005jd006063.

666

667 Liu, C. T., and E. J. Zipser (2009), Implications of the day versus night differences of  
668 water vapor, carbon monoxide, and thin cloud observations near the tropical tropopause,  
669 *Journal of Geophysical Research-Atmospheres*, *114*, 14, DOI: D09303  
670 10.1029/2008jd011524.

671

672 Liu, H. Y., D. J. Jacob, I. Bey, R. M. Yantosca, B. N. Duncan, and G. W. Sachse (2003),  
673 Transport pathways for Asian pollution outflow over the Pacific: Interannual and  
674 seasonal variations, *Journal of Geophysical Research-Atmospheres*, *108*(D20), DOI:  
675 8786 10.1029/2002jd003102.

676

677 Livesey, N. J., W. Van Snyder, W. G. Read, and P. A. Wagner (2006), Retrieval  
678 algorithms for the EOS Microwave Limb Sounder (MLS), *Ieee Transactions on*  
679 *Geoscience and Remote Sensing*, *44*(5), 1144-1155, DOI: 10.1109/tgrs.2006.872327.

680

681 Livesey, N. J., et al. (2007), Earth Observing Systems (EOS) Microwave Limb Sounder  
682 (MLS) Version 2.2 level 2 data quality and description document, version 2.2x-1.0aRep.,  
683 Jet Propulsion Laboratory / California Institute of Technology, Pasadena, California.

684

685 Livesey, N. J., et al. (2008), Validation of Aura Microwave Limb Sounder O-3 and CO  
686 observations in the upper troposphere and lower stratosphere, *Journal of Geophysical*  
687 *Research-Atmospheres*, *113*(D15), DOI: D15s02 10.1029/2007jd008805.

688

689 Mari, C., D. J. Jacob, and P. Bechtold (2000), Transport and scavenging of soluble gases  
690 in a deep convective cloud, *Journal of Geophysical Research-Atmospheres*, 105(D17),  
691 22255-22267.

692

693 McMillan, W. W., C. Barnet, L. Strow, M. T. Chahine, M. L. McCourt, J. X. Warner, P.  
694 C. Novelli, S. Korontzi, E. S. Maddy, and S. Datta (2005), Daily global maps of carbon  
695 monoxide from NASA's Atmospheric Infrared Sounder, *Geophysical Research Letters*,  
696 32(11), DOI: L11801 10.1029/2004gl021821.

697

698 Osterman, G. (editor), et al. (July 31, 2008), Earth Observing System (EOS)  
699 Tropospheric Emission Spectrometer (TES) Level 2 (L2) Data User's Guide (Up to &  
700 including Version F04\_04 data), Jet Propulsion Laboratory, Pasadena, California.

701

702 Park, S., et al. (2007), The CO<sub>2</sub> tracer clock for the Tropical Tropopause Layer,  
703 *Atmospheric Chemistry and Physics*, 7(14), 3989-4000.

704

705 Pickering, K. E., A. M. Thompson, J. R. Scala, W. K. Tao, R. R. Dickerson, and J.  
706 Simpson (1992), FREE TROPOSPHERIC OZONE PRODUCTION FOLLOWING  
707 ENTRAINMENT OF URBAN PLUMES INTO DEEP CONVECTION, *Journal of*  
708 *Geophysical Research-Atmospheres*, 97(D16), 17985-18000.

709

- 710 Poulida, O., R. R. Dickerson, and A. Heymsfield (1996), Stratosphere-troposphere  
711 exchange in a midlatitude mesoscale convective complex, *Journal of Geophysical*  
712 *Research-Atmospheres*, *101*(D3), 6823-6836.
- 713
- 714 Pumphrey, H. C., et al. (2007), Validation of middle-atmosphere carbon monoxide  
715 retrievals from the Microwave Limb Sounder on Aura, *Journal of Geophysical Research-*  
716 *Atmospheres*, *112*(D24), DOI: D24s38 10.1029/2007jd008723.
- 717
- 718 Randel, W. J., and M. Park (2006), Deep convective influence on the Asian summer  
719 monsoon anticyclone and associated tracer variability observed with Atmospheric  
720 Infrared Sounder (AIRS), *Journal of Geophysical Research-Atmospheres*, *111*(D12),  
721 D12314 10.1029/2005jd006490.
- 722
- 723 Ray, E. A., et al. (2004), Evidence of the effect of summertime midlatitude convection on  
724 the subtropical lower stratosphere from CRYSTAL-FACE tracer measurements, *Journal*  
725 *of Geophysical Research-Atmospheres*, *109*(D18), DOI: D18304 10.1029/2004jd004655.
- 726
- 727 Ricaud, P., B. Barret, J. L. Attie, E. Motte, E. Le Flochmoen, H. Teysse, V. H. Peuch,  
728 N. Livesey, A. Lambert, and J. P. Pommereau (2007), Impact of land convection on  
729 troposphere-stratosphere exchange in the tropics, *Atmospheric Chemistry and Physics*,  
730 *7*(21), 5639-5657.
- 731



- 732 Riley, E. M., and B. E. Mapes (2009), Unexpected peak near-15 degrees C in CloudSat  
733 echo top climatology, *Geophysical Research Letters*, 36, 5, DOI: L09819  
734 10.1029/2009gl037558.  
735
- 736 Rossow, W. B., and R. A. Schiffer (1991), ISCCP CLOUD DATA PRODUCTS, *Bulletin*  
737 *of the American Meteorological Society*, 72(1), 2-20.  
738
- 739 Schumacher, C., and R. A. Houze (2003), Stratiform rain in the tropics as seen by the  
740 TRMM precipitation radar, *Journal of Climate*, 16(11), 1739-1756.  
741
- 742 Simpson, J., C. Kummerow, W. K. Tao, and R. F. Adler (1996), On the tropical rainfall  
743 measuring mission (TRMM), *Meteorology and Atmospheric Physics*, 60(1-3), 19-36.  
744
- 745 Strahan, S. E., B. N. Duncan, and P. Hoor (2007), Observationally derived transport  
746 diagnostics for the lowermost stratosphere and their application to the GMI chemistry and  
747 transport model, *Atmospheric Chemistry and Physics*, 7(9), 2435-2445.  
748
- 749 Tian, B. J., B. J. Soden, and X. Q. Wu (2004), Diurnal cycle of convection, clouds, and  
750 water vapor in the tropical upper troposphere: Satellites versus a general circulation  
751 model, *Journal of Geophysical Research-Atmospheres*, 109(D10), 16, DOI: D10101  
752 10.1029/2003jd004117.  
753

754 Waters, J. W., et al. (2006), The Earth Observing System Microwave Limb Sounder  
755 (EOS MLS) on the Aura satellite, *Ieee Transactions on Geoscience and Remote Sensing*,  
756 *44*(5), 1075-1092, DOI: 10.1109/tgrs.2006.873771.

757

758 Wilheit, T., L. J. Allison, and W. Shenk (1973), METEOROLOGICAL  
759 INTERPRETATION OF NIMBUS-5 ELECTRICALLY SCANNING MICROWAVE  
760 RADIOMETER IMAGES, *Bulletin of the American Meteorological Society*, *54*(10),  
761 1117-1117.

762

763 Zhang, G. J., and N. A. McFarlane (1995), SENSITIVITY OF CLIMATE  
764 SIMULATIONS TO THE PARAMETERIZATION OF CUMULUS CONVECTION IN  
765 THE CANADIAN CLIMATE CENTER GENERAL-CIRCULATION MODEL,  
766 *Atmosphere-Ocean*, *33*(3), 407-446.

767

768 Ziemke, J. R., J. Joiner, S. Chandra, P. K. Bhartia, A. Vasilkov, D. P. Haffner, K. Yang,  
769 M. R. Schoeberl, L. Froidevaux, and P. F. Levelt (2009), Ozone mixing ratios inside  
770 tropical deep convective clouds from OMI satellite measurements, *Atmospheric*  
771 *Chemistry and Physics*, *9*(2), 573-583.

772

773 Zuidema, P. (1998), The 600-800-mb minimum in tropical cloudiness observed during  
774 TOGA COARE, *Journal of the Atmospheric Sciences*, *55*(12), 2220-2228.

775

776 Figure Captions

777

778 Figure 1. GMI CO concentrations at middle and upper tropospheric levels, using one  
779 month of daily output between 19°S-19°N. Panel (a) shows values from all grid boxes.  
780 In subsequent panels, values from a grid box are only included if the convective  
781 precipitation rate within that grid box meets the given threshold. The correlation of CO  
782 between the two levels increases as the rain rate increases.

783

784 Figure 2. Each grid box shows the number of days (day count) in July 2007 for which  
785 GEOS-4 computed a tropical convective rain rate satisfying the given threshold, at Aura  
786 afternoon overpass times. Areas of most frequent convective rain correspond with well-  
787 known areas of convection e.g. the ITCZ and the Maritime Continent. In panel (a), rain  
788 rate  $\geq 0.05$  mm/hr, panel (b)  $\geq 0.5$  mm/hr, and panel (c)  $\geq 1$  mm/hr.

789

790 Figure 3. CO concentrations at middle vs. upper tropospheric levels, as measured in the  
791 tropics (18°S-18°N) from Jan 2006 through Dec 2008. TES Global Survey data at 562  
792 hPa were used, only where the Averaging Kernel diagonal was at least 0.085. MLS data  
793 were used at 215 hPa, with values halved to compensate for a factor of 2 bias at this level.  
794 The profiles were screened for quality and cloud presence as described in the text. Panel  
795 (a) shows values from all qualifying profiles. In subsequent panels, a profile is only  
796 included if the maximum local TRMM-based rain rate (within a 3x3 grid patch) meets the  
797 given threshold. As the 3B-42 rain rate threshold increases, so too does the correlation of  
798 CO between the two levels; at the same time, the number of points decreases pretty  
799 dramatically. Histogram insets show the distribution of 1000 bootstrap test correlations,

800 ranging from -1 to 1. Markers below the histograms show the 5%, average, and 95%  
801 locations; markers above show the correlation coefficients using all data.

802

803 Figure 4. Similar to Figure 2; however, this figure shows the geographic distribution of  
804 TES/MLS profile pairs with TRMM rain rates satisfying thresholds 0.0, 0.05 and 1.0  
805 mm/hr (panels (a) and (c) correspond to panels (a) and (b) in Figure 3). The profiles here  
806 are binned at  $2^\circ \times 2.5^\circ$  to match Figure 2. In panel (a), no rain rate threshold is applied,  
807 and the cloud-limiting filter for TES leaves clusters of profiles in areas of very little rain  
808 (e.g. parts of Africa, Saudi Arabia and the South Atlantic). Panels (b) and (c) show the  
809 effects of imposing rain rate thresholds of 0.05 and 1.0 mm/hr; this greatly reduces the  
810 number of profiles, so a different color scale is used. As the required rain rate increases,  
811 the remaining profiles are frequently located near areas of prominent rain (e.g. the ITCZ,  
812 Maritime Continent, and Brazil).

813

814 Figure 5. Correlation of CO measurements from TES (562 hPa) and MLS (215 hPa),  
815 plotted against rain rate thresholds satisfied by TRMM 3B-42. Four methods of rain rate  
816 determination are shown in each panel; they differ only in the number of TRMM values  
817 consulted in the vicinity of the TES/MLS observations, ranging from 77 (11x7) down to  
818 9 (3x3). Each panel imposes a different AKD minimum for the TES data: 0.08, 0.085 and  
819 0.09. Data spans three full years, 2006-2008. The points on the red/asterisk line (3x3  
820 patches) in panel (b) correspond to the correlation coefficients shown in Table 1.  
821 Correlation is not recorded if it does not satisfy the bootstrap criteria described in section  
822 3.2.1.

823

824 Tables

825

826

Rain Rate Threshold (mm/hr)	0	0.5	1.0	1.5	2.0	2.5	3.0
Correlation Coefficient	0.454	0.538	0.604	0.618	0.719	0.780	0.804
Profile count	9940	213	108	64	45	33	22

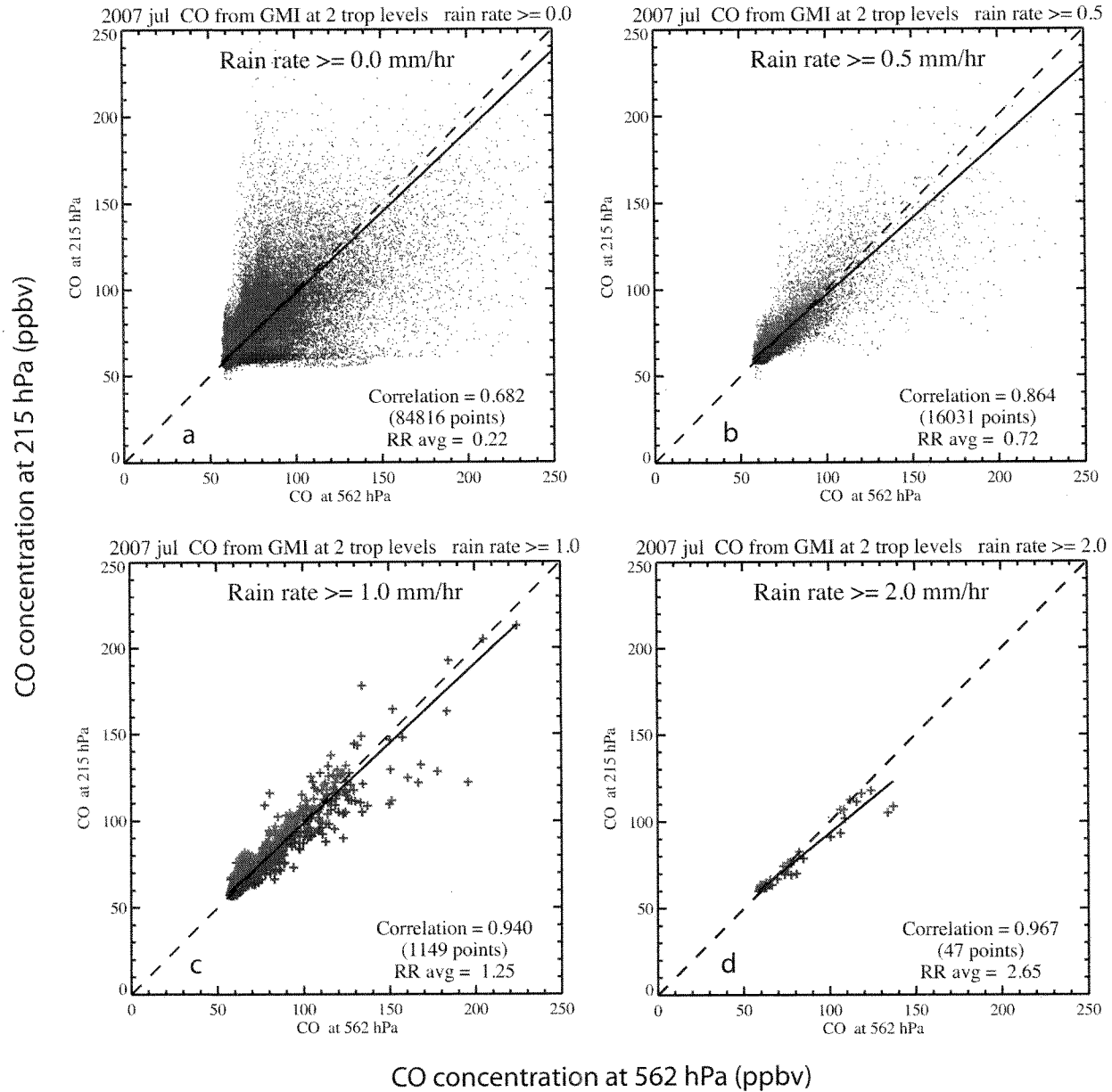
827

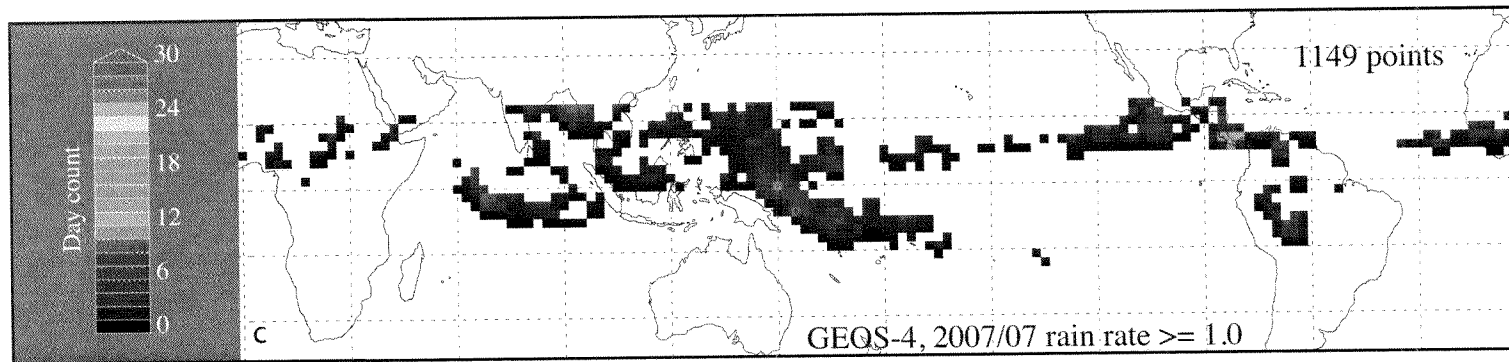
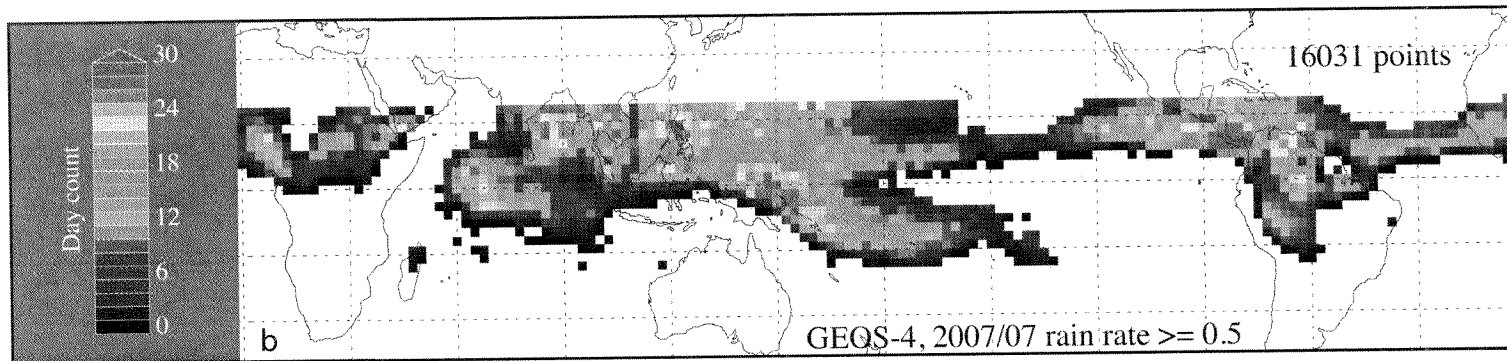
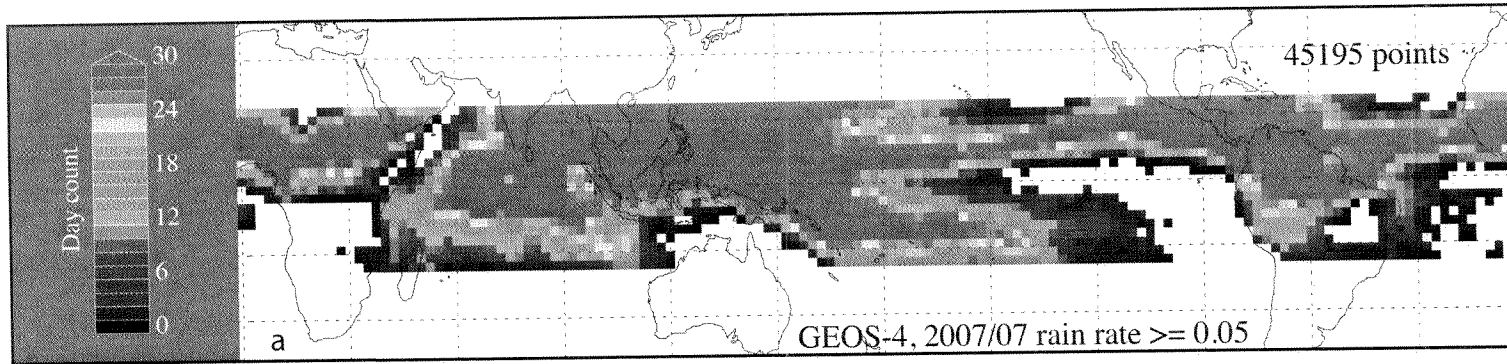
828 Table 1. Interlevel CO Correlation Coefficients

829 CO correlations between middle and upper tropospheric levels associated with various

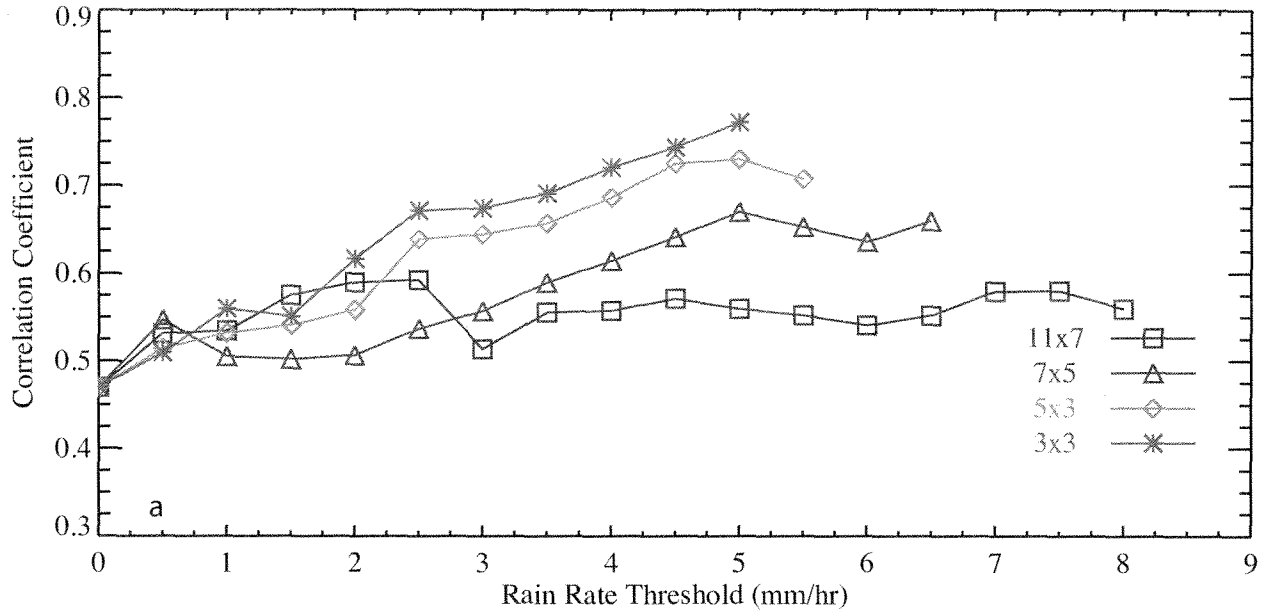
830 rain rate thresholds. Cases shown include those from Figure 3 along with intermediate

831 rain thresholds.

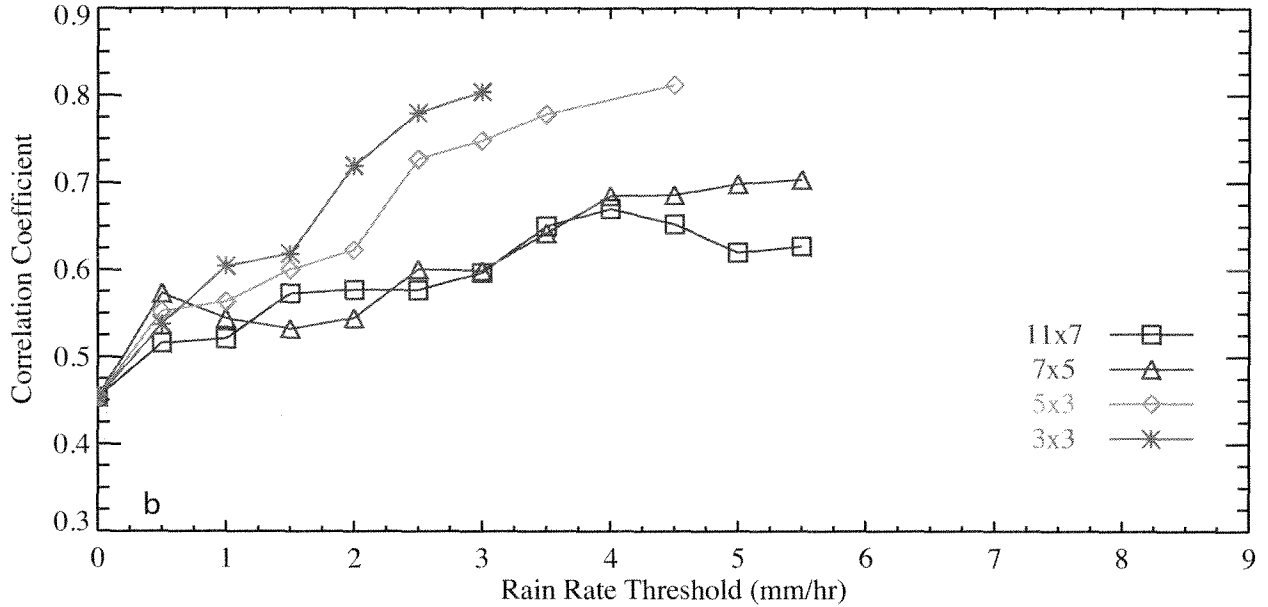




TES/MLS CO at 562 & 215 hPa, TES akd  $\geq 0.080$



TES/MLS CO at 562 & 215 hPa, TES akd  $\geq 0.085$



TES/MLS CO at 562 & 215 hPa, TES akd  $\geq 0.090$

